Applications of Magnetic Resonance Cytography:

Assessing Underlying Cytoarchitecture

by

Alberto Enrique Fuentes

A Thesis Presented in Partial Fulfillment
of the Requirements for the Degree
Master of Science

Approved November 2018 by the
Graduate Supervisory Committee:

Chad C. Quarles, Co-Chair
Vikram Kodibagkar, Co-Chair
Bradley Greger

ARIZONA STATE UNIVERSITY

December 2018

ABSTRACT

In medical imaging, a wide variety of methods are used to interrogate structural and physiological differences between soft tissues. One of the most ubiquitous methods in clinical practice is Magnetic Resonance Imaging (MRI), which has the advantage of limited invasiveness, soft tissue discrimination, and adequate volumetric resolution. A myriad of advanced MRI methods exists to investigate the microstructural, physiologic and metabolic characteristics of tissue. For example, Dynamic Contrast Enhanced (DCE) and Dynamic Susceptibility Contrast (DSC) MRI non-invasively interrogates the dynamic passage of an exogenously administered MRI contrast agent through tissue to quantify local tracer kinetic properties like blood flow, vascular permeability and tissue compartmental volume fractions. Recently, an improved understanding of the biophysical basis of DSC-MRI signals in brain tumors revealed a new approach to derive multiple quantitative biomarkers that identify intrinsic sub-voxel cellular and vascular microstructure that can be used differentiate tumor sub-types. One of these characteristic biomarkers called Transverse Relaxivity at Tracer Equilibrium (TRATE), utilizes a combination of DCE and DSC techniques to compute a steady-state metric which is particularly sensitive to cell size, density, and packing properties. This work seeks to investigate the sensitivity and potential utility of TRATE in a range of disease states including Glioblastomas, Amyotrophic Lateral Sclerosis (ALS), and Duchenne's Muscular Dystrophy (DMD). The MRC measures of TRATE showed the most promise in mouse models of ALS where TRATE values decreased with disease progression, a finding that correlated with reductions in myofiber size and area, as quantified by immunohistochemistry. In the animal models of cancer and DMD, TRATE results were

more inconclusive, due to marked heterogeneity across animals and treatment state. Overall, TRATE seems to be a promising new biomarker but still needs further methodological refinement due to its sensitivity to contrast to noise and further characterization owing to its non-specificity with respect to multiple cellular features (e.g. size, density, heterogeneity) that complicate interpretation.

ACKNOWLEDGMENTS

I'd sincerely like to thank Chad C. Quarles for giving me the opportunity to participate in the incredible research being done at the Barrow Neuroimaging Innovation Center. In addition, I'd like to thank him for the countless mentoring sessions and guidance during my research. I'd also like to thank my seniors in the lab Laura C. Bell, Ashley M. Stokes, Nathaniel B. Semmineh, and Sudarshan Ragunathan for their brilliant and patient guidance. I'd also like to thank the Pre-Clinical imaging Core's Gregory Turner and Xiaowei Zhang for their support and assistance. Last but not least, I sincerely thank our Lab Technician Deborah Healey for the wonderful histology provided to accompany this work.

I've learned so much over the past two years, and never would think I was capable of this level research. But, thank you so much to everyone involved for allowing me to grow and your encouragement. For this, I'd like to thank Dr. Quarles and to everyone in the Neuroimaging Innovation Center again.

Part of this work was funded by the Flinn Foundation as part of ALS research grant for the development of ALS Imaging biomarkers.

TABLE OF CONTENTS

Page

Page

LIST OF FIGURES

CHAPTER 1
INTRODUCTION

Magnetic Resonance Imaging Basics

Over the course of recent decades advances in medical imaging has created new opportunities to non-invasively interrogate the human body. One of the most prominent and ubiquitous methods is Magnetic Resonance Imaging (MRI), developed in the 1970s stemming from earlier research in physics investigating the polarization of nuclear spins, like protons, and their net magnetization when placed in a strong magnetic field as well as their response to radiofrequency (RF) radiation [1]. In general, MRI relies on the excitation of spins using radiofrequency pulses and detection of the subsequent RF radiation that occurs during spin relaxation. The proton signal is measured via a RF coil, leveraging Faraday's Law of Induction. Spatial localization can be achieved through the application of magnetic gradient fields that introduce spatially dependent frequency and phase of proton spins in a main magnetic field. After these perturbations, the recovery, also known as the relaxation, of the protons depends on the specific characteristics of the local proton environment and tissue composition. Since the body is comprised of 90% water molecules from soft tissues that are diverse in chemical structure and composition, it is possible to discriminate between soft tissues based on the proton populations in each tissue. For example, consider the difference in proton concentration between the cerebrospinal fluid (CSF) and grey matter. In the CSF, a high proportion of hydrogen protons are present due to the fluid which provides a brighter signal compared to the grey matter containing a lower proportion of protons. In addition to soft tissue discrimination,

advance MRI techniques allow for the interrogation of factors such as water movement, chemical composition, and hemodynamic properties.

Before continuing to more advance techniques such as dynamic contrast imaging, it is useful to review the concepts of relaxation first. In the presence of a large magnetic field the magnetic moments of proton spins will align creating a net magnetization that is preferentially aligned in the direction of the applied field. After application of the RF pulse, the net magnetization is rotated away from this main field, which is conventionally defined as the Z-direction, and into the transverse (X-Y) plane. In MRI there are two main types of relaxation observed and measured as the net magnetization recovers to equilibrium. First, T_1 relaxation, or longitudinal relaxation time, characterizes the rate at which the net magnetization recovers to the original magnitude and alignment along the Z-axis prior to perturbation. As shown in Figure 1.1 the recovery of the Z-magnetization as a function of time after the application of the RF pulse (a) as well as the equation characterizing the relaxation (b).

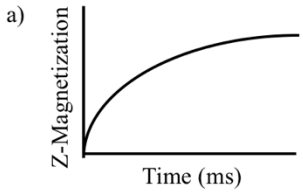

b)

$$M_z = M_{z0}\left[1 - \exp\left(\frac{-t}{T_1}\right)\right]$$

Figure 1.1 -Example of T_1 Evolution with governing Equations

Biophysically, T_1 relaxation occurs as the system of protons lose the energy imparted through the RF pulse and, accordingly, can be considered thermal relaxation. The energy is transferred to surrounding molecules in the external environment through collisions

and other electromagnetic interactions. The efficiency of this energy loss depends on the local biochemical composition of the tissue [2]. T_1 weighted imaging is often used to determine structural and anatomic characteristics of tissue such as bulk atrophy in muscle and cerebellum, and cortical thickness of grey matter in the brain [2-4].

The second type of relaxation is T_2 relaxation, which characterizes the rate of the decay of the magnetization in the transverse (X-Y) plane of signal. Biophysically, T_2 relaxation occurs through spin-spin interactions, diffusion and dephasing in the presence of local (microscopic) static field disturbances. In practice, the transverse magnetization decays much faster than dictated by T_2 due to macroscopic field inhomogeneities or susceptibility induced field distortions. Thus, the observed T_2 is defined as T_2* and both times can be quantified through appropriate pulse sequence design. The general time course for T_2 decay can be seen in Figure 1.2.

a)

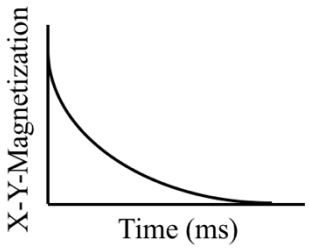

b)

$$M_{xy} = M_{xy0}\left[\exp\left(\frac{-t}{T_2}\right)\right]$$

Figure 1.2 - Example of T_2 Decay with governing Equations

The T_1, T_2, and T_2* relaxation times are the primary contrast mechanisms leveraged in the vast majority of clinical imaging. The times can be quantified through specialized pulse sequences that repeatedly sample the signal recovery (in the case of T_1) or decay (in

the case of T_2 and T_2*) over time. The resulting time profiles can be fit to well established logarithmic models of the decay(T_2/T_2*) or recovery (T_1).

While these relaxation mechanisms are used to generate soft-tissue contrast in anatomic MR, the underlying biophysical basis of MR spin physics and contrast mechanism affords numerous opportunities to interrogate many additional relevant biological features. Key techniques used in clinical and research practice are MR Spectroscopy (MRS), Diffusion Imaging, functional MRI (fMRI), and Perfusion Imaging. In each of these sub-types there are a diverse set of techniques to glean more information from the proton signal. For example, consider diffusion imaging in which the voxel-wise Brownian motion of water movement can be measured by acquiring images with specially designed diffusion sensitive gradients [2]. Diffusion Imaging can also be leveraged to visualize white matter fiber tracks using the method known as Diffusion Tensor Imaging. Magnetic resonance spectroscopy can be used to interrogate the chemical composition within tissue by analyzing the chemical shift of molecules that have detectable spins (e.g. 1H, 31P, 13C). The MRS technique has been particularly useful in analyzing brain tumor environments and progression through monitoring of Choline (Cho) and N-acetyl aspartate (NAA) levels and ratios [5]. MRI is not only limited to assessing inherent features. With fMRI, composite changes in local blood oxygenation, blood flow and blood volume in response to different brain states or response to stimuli can be evaluated through dynamic measures of T_2*-weighted MRI signals. With this technique it is possible to map specific regions of activation in relation to speech and language to aid in determining resection boundaries for surgery.

It is the combination of all these techniques, that is used in current clinical practice and research. Unlike most other imaging modalities, MRI is able to provide a more comprehensive assessment of tissue anatomy, microstructure, physiology and biochemical composition, enabling physicians to make more confident diagnosis and plans of care. The extraordinary range of contrast mechanisms provided by MRI also serves as the basis for the development and application of novel biomarkers investigated in the studies described herein.

Perfusion Imaging Basics

Dynamic imaging is often used to characterize the changes in a tissue's MRI signal over time as paramagnetic contrast agent flows through the vasculature, into the extravascular space and back again. Intrinsic heterogeneity and pathology-induced changes in tissue microstructure give rise to differences in local contrast agent kinetics. Original work conducted in 1987 by Villrigner and colleges showed with T_2 weighted imaging as Gd(DPTA)2- passed through the capillaries that the MRI signal intensity decreases [6]. This effect was determined to be caused by a difference between the magnetic susceptibility between the capillaries containing contrast and the surrounding tissue, inducing field gradients that decreased spin phase coherence and T2* [6]. This gave rise to the field that is now called Dynamic Susceptibility Contrast (DSC) MRI, which continues to leverage contrast agent induced signal decreases to interrogate local hemodynamics, primarily in the brain. Alternatively, it is possible to use Dynamic Contrast Enhanced (DCE) MRI which involves a T_1 weighted imaging approach to detect concentrations of paramagnetic contrast agent and its dynamic passage through tissue. By utilizing the shortening effects of contrast agents on T_1 relaxation it possible to detect

differences in the physiology and pathology of the tissue after the contrast agent is allowed to interact with the local environment causing an increase in signal intensity from the shortened T_1 recovery [7].

An important consideration for both DSC-MRI and DCE-MRI are the quantitative tools that are needed to determine parameters such as concentration, Cerebral Blood Flow (CBF), Cerebral Blood Volume (CBV), Mean Transit Time (MTT), vascular permeability and/or the volume fraction of the extravascular, extracellular space (EES). For both methods these parameters can be extracted by applying pharmacokinetic models of tracer passage through the tissues of interest. Many of these models consider an array of hemodynamics features that can change the observed curve such as transfer of contrast agent between intravascular, extravascular, intracellular, and extracellular compartments [7-10]. Figure 1.2 shows an example two compartment model of contrast agent passage in the vasculature. Where k_{in} and k_{out} are the rate constants characterizing the influx and efflux of contrast agent into the system. The $k_{1,2}$ and $k_{2,1}$ transfer constants describe the passage of contrast agent between EES and blood-plasma.

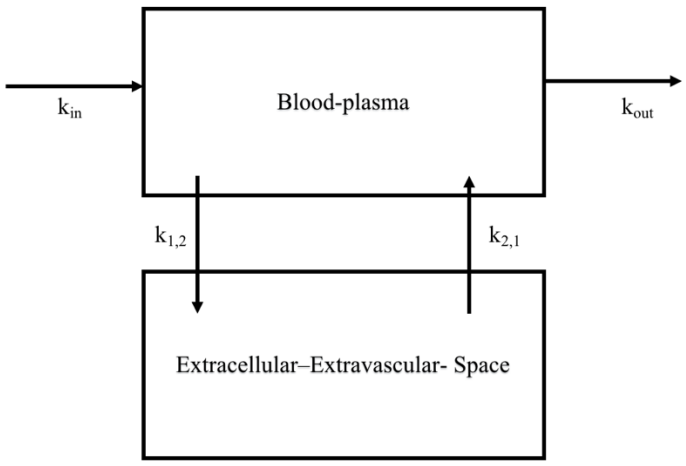

Figure 1.3– Generic Two Compartment Model of Tracer Kinetics

Another important caveat of perfusion imaging with MRI is that, as a modality, it does not directly detect the administered contrast agent. Rather, it detects the influence of the contrast agent on the intrinsic MR relaxation times. Consequently, in order to measure the voxel-wise contrast concentration it is necessary to characterize the relationship between the relaxivity of the tracer and the change in longitudinal and/or transverse relaxation rate ΔR_1 and ΔR_2, where $R_1 = 1/T_1$ and $R_2 = 1/T_2$ [7]. As an example, Equation 1.1 shows the relationship between contrast agent concentration, R_1 relaxation rate change, and the contrast agent relaxivity, where C(t) is the concentration in a given voxel at a point in time after contrast has been injected, $R_1(t)$ is the relaxation rate time profile, r_1 is the longitudinal relaxivity of the contrast agent, and R_{10} is the baseline or pre-contrast longitudinal relaxation rate. Note that r_1 is a constant that defines how effective a contrast agent is at inducing changes in T_1. A similar constant and relationship can be described for contrast agent based T_2 relaxation ranges.

$$R_1(t) = r_1 \cdot C(t) + R_{10} \qquad \text{(Eq.1.1)}$$

A feature that is unique to MRI is that it is not only limited to interrogating the passage of contrast agent for hemodynamic characterization, but it can also be used to glean inherent microstructural and morphological differences due to the biophysical basis of susceptibility-based contrast mechanisms. For example, by utilizing the contrast-agent changes in R_2 and R_2* it possible to obtain measures of mean vessel size in a voxel as shown by Tropès group [11]. Sensitivity to these structural characteristics originate from the susceptibility differences between tissue compartments (e.g. blood vessels and the EES), their volume fractions, their architecture and the induced magnetic field changes in response to contrast agent. As theorized by Yablonskiy and Haacke, the resulting signal

observed has a dependence on volume fraction, susceptibility of the medium and objects, local magnetic field, and the main magnetic field [12]. A subtlety to susceptibility contrast MRI methods involves the sensitivity of spin echo (SE) and gradient echo (GRE) pulse sequences to the radius of the underlying structures (e.g. vessels). Specifically, Kiselev et al. showed in Monte Carlo simulations that GRE sequences are sensitive to vessels of all sizes, whereas SE sequences are maximally sensitive to capillary sized vessels. [28]. The advantage of combining the two echo sequences provides a sensitivity to both large vessel and small vessel radii and enables interrogation of mean vessel size in a voxel.

The fields of DCE-MRI and DSC-MRI continue to push forward in utilizing innovations in hardware and pulse sequence design to allow for improved spatial and temporal resolution, extraction of new biomarkers, and standardizing acquisition and post-processing approaches to generate more reliable and reproducible results [13-14]. These efforts have increased the general use of these methods in both clinical practice and research, particularly in the fields of cancer and stroke imaging. With the increased availability of higher field MRI, improved biophysical characterization of contrast mechanism and development of and new types of contrast agents it is expected that this mature field will continue to experience the development of new methodologies and techniques.

Magnetic Resonance Cytography

Historically, biophysical consideration of DSC-MRI contrast mechanisms focuses on the impact of contrast agents confined within vascular structures, because it is assumed that contrast agents do not extravasate. While this is typically true in normal brain, in

pathologies like cancer, the BBB is disrupted as part of the tumor angiogenic process. When this occurs the contrast agent is dynamically distributed between the vasculature and extravascular extracellular space. This contrast agent redistribution and its impact on perfusion measures required a new theoretical investigation in order to understand the factors that influenced the acquired DSC-MRI signals [15-16]. These efforts revealed that DSC-MRI data in tissues with a disrupted BBB are heavily influenced by both the vascular structure as well as the cellular microstructure (e.g. cell size, spacing, density, etc) [17]. This sensitivity to cellular features formed the underlying basis for what we now term Magnetic Resonance Cytography.

Quarles et al developed a heuristical analytic model that characterizes the factors that contribute to ΔR_2* data collected in brain tumors, including the extravascular extracellular (EES), extravascular intracellular (EIS), vascular space, the contrast agent concentration in each compartment, T_2 contrast agent relaxivity, and the T_2* contrast agent relaxivity that accounts for the microstructural properties of the vascular and extravascular compartment [15]. Soon after the administration of contrast agent, the concentration in the vascular space (C_p) and extravascular extracellular space (C_e) will be different. But after some time, the tissue of interest reaches a steady-state where C_p and C_e reach equilibrium [17]. At equilibrium (when Cp = Ce) there is no longer a susceptibility difference between the vascular and extravascular space and they are effectively as a single compartment, whose structure is defined by the three-dimensional distribution of cells. Note that clinical MRI contrast agents do not enter cells so there always remains a susceptibility difference between the vasculature and/or EES and the EIS. Another benefit of focusing on equilibrium is that we only need to consider the total

tissue contrast agent concentration rather than trying to separately measure the concentration in the vessels and in the EES. At equilibrium, the R_2* simplifies to Equation 1.2, and is a function of tissue contrast agent concentration, volume fractions, and compartmentalized relaxivities, where, r_2 is the T_2 relaxivity of the contrast agent, v_i is the EIS volume fraction, v_e is the EES volume fraction, v_p is the vascular volume fraction, r^*_{2p} and r^*_{2e} are the T_2* relaxivities of contrast agent in the vascular space and EES respectively, and C_t is the concentration in the voxel [17].

$$\Delta R2^* = \left\{ r_2 + \frac{v_i}{v_p + v_e} \left(v_p r^*_{2p} + v_e r^*_{2e} \right) \right\} C_t \qquad \text{(Eq. 1.2)}$$

The bracketed term in Equation 1.2 consists only of static terms and serves as an effective transverse relaxivity that we term the transverse relaxivity at tracer equilibrium ($r^*_{2t,eq}$) or TRATE [17]. With this notation TRATE can be computed as:

$$TRATE = r^*_{2t,eq} = \frac{\Delta R^*_2}{C_t} \qquad \text{(Eq. 1.3)}$$

Experimentally, a specialized MRI protocol needs to be employed (beyond straightforward single-echo DSC-MRI) for MRC measures of TRATE, which requires the simultaneous quantification of ΔR_2* (that is free of T_1 effects) and ΔR_1 so that C_t can be directly measured, using the conventional notation found in DCE-MRI ($C_t = \Delta R_1 / r_1$). To simultaneously measure ΔR_2* and ΔR_1 we can utilize a dynamic multi-echo acquisition strategy and also collect a pre-contrast T_1 map.

Using computational simulations, Semmineh et al. showed that TRATE is highly sensitive to variations in cell size and density. With in-vivo data and ex-vivo histologic validation, TRATE was found to significantly differ between brain tumor animal models that exhibit dissimilar cellular features. These initial efforts provided the basis for the use

of TRATE as a biomarker of cytographic features in a range of pathologies and organs, as evaluated herein.

CHAPTER 2

AMYOTROPHIC LATERAL SCLEROSIS MODEL

Disease Introduction

Amyotrophic Lateral Sclerosis (ALS), also known as Lou Gehrig's disease, is a neurodegenerative disease characterized by the progressive loss of upper and lower motor neuron function. This loss of function leads to symptoms such as muscular weakness and abnormalities early on, then developing into fatal difficulty of breathing and swallowing [16,17]. ALS prevalence is 5 cases per 100,000 in the U.S, this may be due to longer life expectancies and increased awareness of the disease from advances in medicine [16,18]. From onset, the life expectancy of patients tends to be 30 months to 5-10 years and varies depending on the type, and anatomic location of onset atrophy [19]. Even so, there are many therapies in development and ongoing research that is aimed at stopping degeneration of motor neurons or halting the process to extend lifespans [18].

Biomarkers for ALS have been difficult to find and implement [16]. Current diagnostic techniques involve electro-conductivity studies, cerebrospinal fluid analysis, and neuroimaging [16,20]. Imaging techniques range from analysis of the structure of cortico-spinal tracts, cortical thickness and volumetric measurement of the afflicted muscle [16,20-23,26]. These techniques include analyzing the differences between healthy and diseased tissue utilizing T_2 and T_2* weighted magnetic resonance imaging (MRI) for identifying fat infiltration and ADC [24,25]. In similar disease states where muscle dystrophy occurs, MRI has been used to study structural changes associated with muscle degeneration [26,27].

When considering the physiological effects of this disease it is important to understand what atrophy does to muscles. Muscle atrophy is considered an active process controlled by signaling pathways, in which degradation of muscle growth factors that are used in protein synthesis are targeted [29]. Complex signaling pathways and factors are involved in normal muscle growth, but in muscular atrophy there are many signaling factors that are either inhibited or missing leading to a decrease muscle mass, myo-fiber size, and their distribution [29]. In ALS, the loss of α-motor neuron signaling leading to atrophy occurs at later stages of the disease where symptoms are already onset, detecting the progression of this atrophy is important for prognosis and quality of care. This detection of atrophy, is a prime opportunity for TRATE to be utilized for the assessment of myofiber changes.

Methods

Animal Model

In this study 8 SOD1 mice with strain B6.Cg-Tg(SOD1*G93A)1Gur/J and 8 Control mice where obtained from Jackson Laboratories. The mice were then imaged at 9 weeks, 12 weeks, and 15 weeks old to observe onset to late stage progression. All experiments and care for the mice were carried out in accordance with our institution's animal care and use polices. At each time point a control mouse and an ALS mouse were sacrificed for histology. Histological analysis was used to quantify the distribution of myofiber diameters, and myofiber area and number.

Image Acquisition

The mice were imaged with a 7 Tesla Bruker Scanner utilizing a 72mm transmit and read volume coil. Similar to the protocol applied in Semmineh et al. a pre-contrast T_1

images was acquired using a Variable Recovery Time (VTR) sequence with parameters: Repetition Time (TR) = [350ms, 500ms, 1000ms, 1500ms, 3000ms, 5000ms], Echo Time (TE) = 11ms, Field of View (FOV) = 30 mm^2, Slice Thickness = 1.5mm, Flip Angle (FA) = 90°, Matrix = 150x150x6. Once the T_1 was acquired, we collected dynamic MRC data using a multi-Echo gradient and spin echo sampling of the FID (GESFIDE) with the following parameters: TR = 350ms, 8 Echoes with spacing 1.96ms with start TE_1 = 2.4ms and end TE_8 = 23.7ms, FOV = 30mm^2, Slice Thickness = 1.5mm, FA = 90°, Dynamics = 40, Matrix = 98x98x6x40. A 0.2mM/kg dose of Gadavist (0.1mM/mL concentration) was administered after the 5th dynamic. To administer the contrast agent, a tail vein catheterization was performed to allow for an injection administered from a Genie Touch Syringe Pump (Lucca Technologies) at a rate of 1ml/min. MRC data was acquired for a total of 22 minutes after contrast agent injection. A GRE and SE sequence was utilized in order to determine, for the first time, if spin echo based TRATE values could be detected in muscle tissues. We focused our analysis in this study on the GRE data.

Data Analysis

In order to obtain relevant T_2, T_2*, and T_1 values, scans underwent a voxel-wise non-linear fitting utilizing a Levenberg-Marquardt algorithm with MATLAB's built-in *lsqcurvefit* function to determine relaxation values. In the case of the T_1 VTR scan, the resulting pre-contrast T_1 map was used to obtain dynamic T_1 values from the GESFIDE sequence. By utilizing the spoiled gradient recalled equation to find instantaneous R_1 a dynamic curve can be obtained from the first echo of the DSC signal, which has minimal T_2* contribution [10]. Calculation of pre-contrast T_1 signal S_0 from the GESFIDE sequence is shown in equation 2.1 where α is Flip Angle, TR is repetition time of the

GESFIDE sequence, S_ is average baseline signal from the GESFIDE of the first echo TE_1, and T_1 is the pre-contrast T_1 map.

$$S_0 = S_- \frac{\left[\left(1-e^{-\frac{TR}{T_1}}\cos\alpha\right)\right]}{\left[\left(1-e^{-\frac{TR}{T_1}}\right)*(\sin\alpha)\right]} \quad \text{(Eq. 2.1)}$$

From this calculation we can obtain an instantaneous R_1 value at each dynamic to calculate a ΔR_1 value in given voxel with the TE_1 signal of the GESFIDE sequence at each time timepoint t.

$$R1(t) = \frac{-1}{TR}\ln\left(\frac{S(t)\cos\alpha - S_0\sin\alpha}{S(t) - S_0\sin\alpha}\right) \quad \text{(Eq. 2.2)}$$

With ΔR_1 values we can use Equation 1.1 and the r_1 relaxivity for Gadavist to calculate the concentration (C_t) in the voxel at each dynamic. By utilizing the last 5 dynamics of the GESFIDE data (approximately four minutes) as our equilibrium time frame we are able to calculate voxel-wise TRATE with Equation 1.3. To ensure data quality, thresholds are applied for specific signal to noise ratios (SNR) and contrast to noise ratio (CNR) minimums. Regions of Interests (ROI) were drawn to encompass the whole gastrocnemius, lateral gastrocnemius, and medial gastrocnemius making sure to avoid bone.

Results

Figure 2.1 shows the extracted concentration and ΔR_2* dynamic time profiles in 15-week-old SOD1 and control mice. These curves are averaged across voxels in the whole gastrocnemius muscle. Note that the magnitude of the curves are not necessarily due to physiological differences but because of an unexpected experimental confound that led to dose variability. This dose variability does not confound the estimation of TRATE

(assuming sufficient CNR) because its calculation accounts for the delivered dose. It is important to note from these curves that we see robust concentration and ΔR_2^* values at time points well past the initial tracer delivery (e.g. >15 minutes) where equilibrium can reasonably be expected. It is also important to distinguish that equilibrium does not necessarily imply a constant C_t but rather that Cp = Ce.

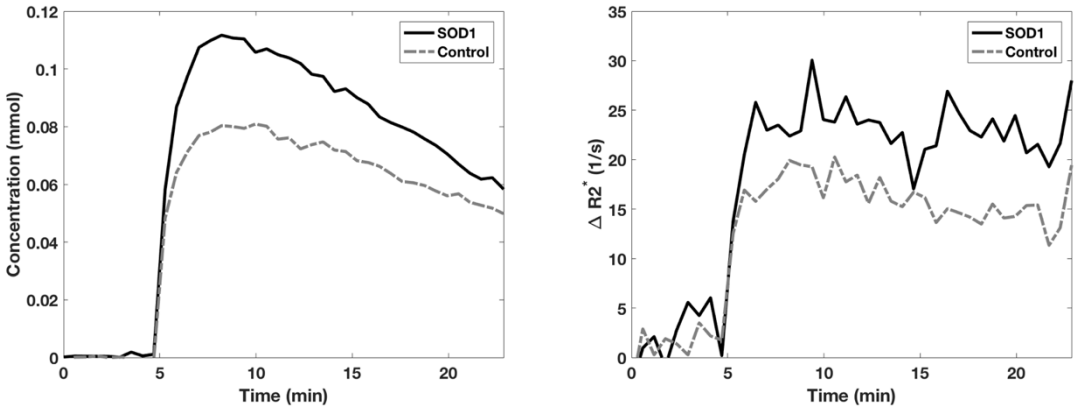

Figure 2.1 – Comparison of characteristic concentration and ΔR_2^* curves in the gastrocnemius muscle

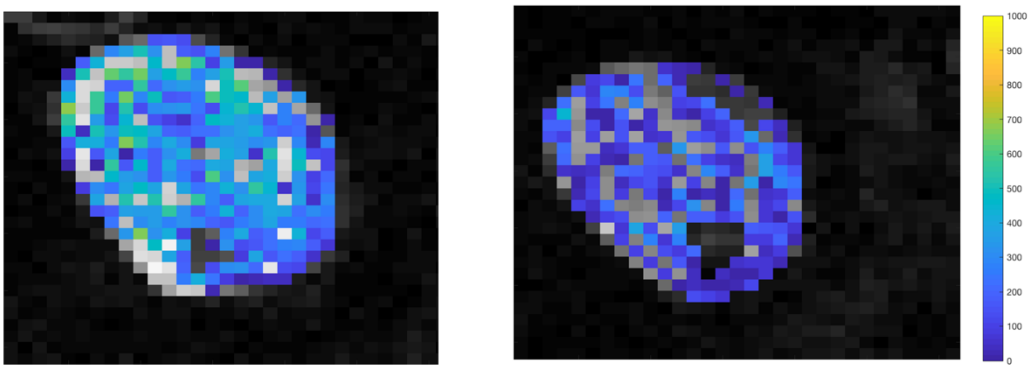

Figure 2.2 – Comparison of TRATE maps of the Gastrocnemius

In Figure 2.2 we see the spatial distribution of TRATE values in the gastrocnemius between a characteristic control and ALS mouse at 12-weeks-old where the range is from 0-1000 $(mmol\text{-}s)^{-1}$. Colored voxels are the voxels with reasonable SNR and CNR to be used in comparisons. Two main observations are that in both control and ALS mice the distribution of TRATE values is very heterogenous, and that there appears to be a larger amount of high TRATE values in the control mice when compared to the ALS mice.

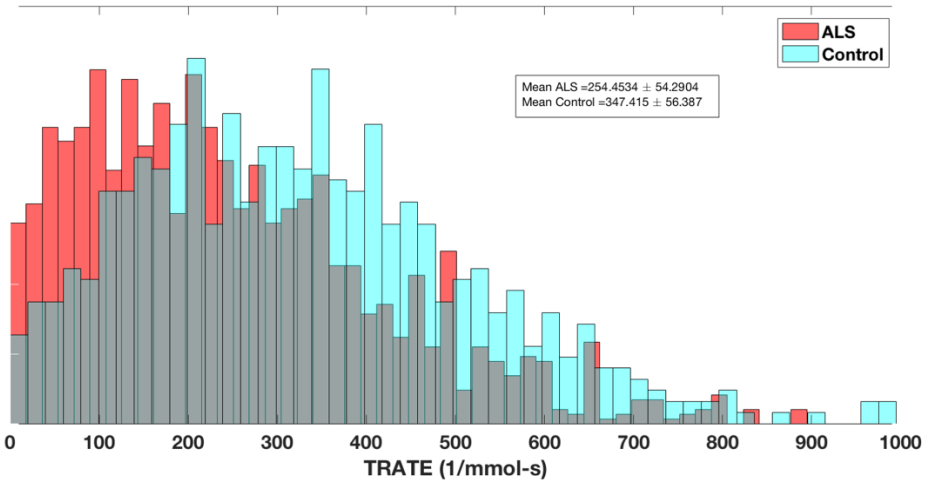

Figure 2.3 – Histogram distribution of TRATE values at 15-Weeks

Figure 2.3 illustrates the histogram of TRATE values in 15-week-old control and ALS mice across all voxels. Note the shift in the ALS mice towards lower TRATE values as compared to controls which are centered around 300 $(mmol\text{-}s)^{-1}$.

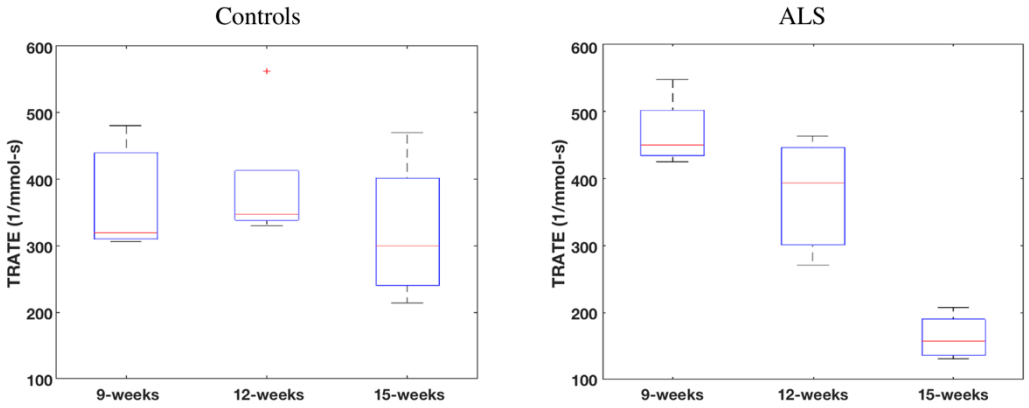

Figure 2.4 – Boxplot of Average TRATE Values Over Time

Figure 2.4 shows the range of TRATE values in 9-week, 12-week, and 15-week old control mice, most commonly varied between 300 to 400 $(\text{mmol-s})^{-1}$. As expected, TRATE values remained constant over the course of the study ($p = 0.483$). It is critically important to note that the magnitude of these TRATE values far exceed to reported T_2 relaxivity of Gadovist (~ 4 $(\text{mmol-s})^{-1}$), indicating that the measured T_2* effects are originating from the much stronger susceptibility effects that give rise to TRATE. The TRATE values in the ALS group at 9 weeks were comparable to controls (which is consistent with known histopathology) but are observed to decrease significantly over time ($p = 0.003$), with values ranging from 100 – 200 $(\text{mmol-s})^{-1}$ at 15 weeks. Sample sizes were 9-weeks (Control n = 8, ALS n = 8), 12-weeks (Control n = 5, ALS = 6), and 15-weeks (Control n = 4, ALS = 5).

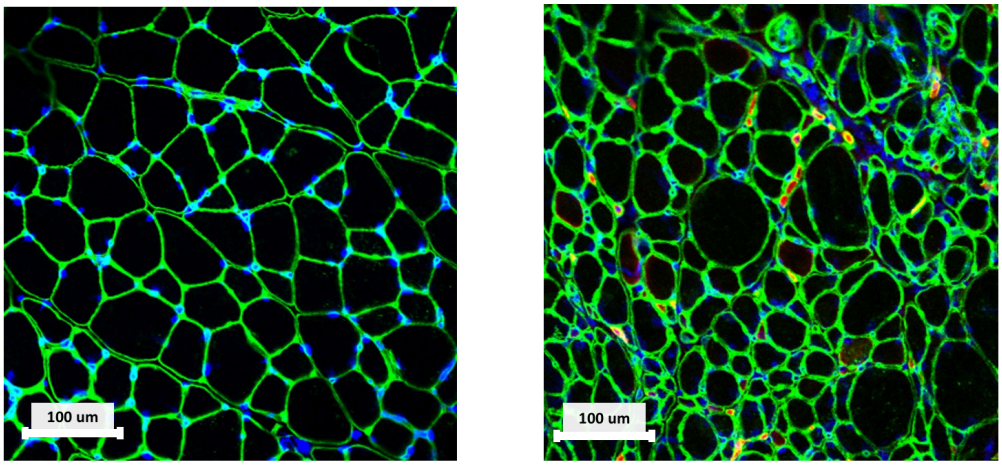

Control ALS

Figure 2.5- Immunofluorescence Imaging of Muscle Sample using DAPI (Blue), Laminin(Green), and Heavy Chain Myosin Stain (Red).

Figure 2.5 shows Immunofluorescence DAPI, and CD98 antibodies staining for nuclei and plasma membrane of myofibers in the gastrocnemius at 15-weeks of disease progression. As compared to control mice, the myofibers in ALS mice were smaller in diameter and much less uniform. Figure 2.6 shows the quantitative analysis of individual myofiber data and further confirms the reduction in cell area and minimum fiber diameter.

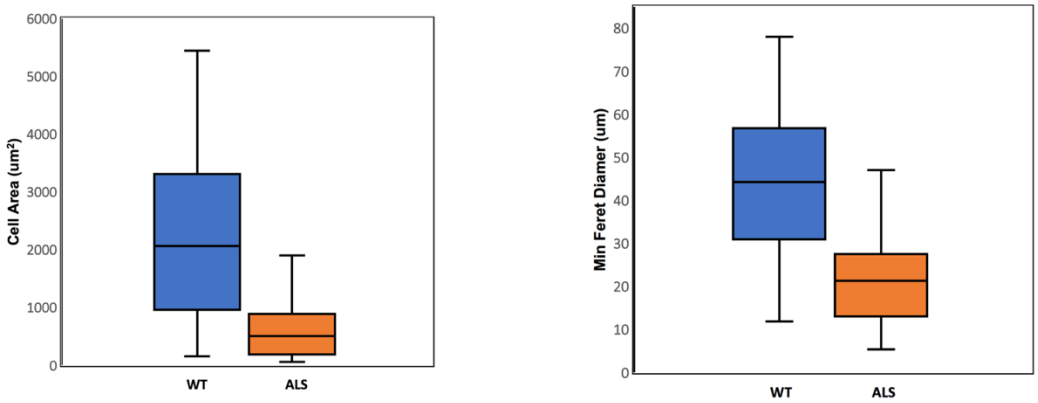

Figure 2.6 – Histologic Analysis of Cell Area and Minimum fiber diameter.

Discussion

These results indicate that TRATE is sufficiently sensitive to tissue cytographic features such that it is able to detect progressive myofiber degeneration in mouse models of ALS. Histological analysis confirmed the expected reductions in myofiber area and size, and provide a mechanistic underpinning for the measured TRATE changes. These results are also consistent with previous simulations in our lab demonstrating that TRATE decreases with cell size.

As this was the first application of MRC outside the brain a number of experimental challenges were observed and had to be overcome. First, as noted above, tail vein bolus injections yielded highly variable doses across mice, which was confirmed by investigating contrast agent concentration in voxels within arterial vessels. In cases where the dose was lower than desired, the CNR within muscle was, at times, prohibitive for MRC analysis, requiring the development of systematic voxel-wise quality control measures. These measures ensured that only voxels exhibiting robust T_1 and T_2* changes were considered for analysis. In the next round of experiments, we are addressing this issue using a continuous infusion approach with a predetermined contrast agent concentration threshold within the muscle as a stopping point for the infusion.

Another challenge presented in the ALS mouse was reliable methods for ROI delineation due to the progressive degeneration and wasting of the muscle, resulting in substantially reduced muscle volumes. Finally, we expect that a potential source of the marked (and unexpected) heterogeneity in TRATE values in both control and ALS mice is the spatially dependent orientation of individual myofibers with respect to the main

magnetic field. Biophysically, it is well known that magnetic fields surrounding perturbers, like a long cylinder, are dependent on the angle of the perturber with respect to the applied field. The orientation dependency could be exacerbated if the legs of each animal were not reproducibility positioned during each scan. Future studies will seek to explore the biophysical basis of this as it would inform future clinical implementation.

Conclusion

The results of this longitudinal experiment support the use of TRATE as a biomarker for muscle atrophy in a preclinical model of ALS. Further work is needed to identify when TRATE is able to identify the earlier stages of muscle degeneration. Histological analysis indicates that TRATE changes originate, in part, from reduced myofiber size. Further validation of TRATE's sensitivity to muscle degeneration would enable the use of MRC as a biomarker for preclinical pharmaceutical and biologic therapy targeting atrophy. Moving forward, it will be important to combine this technique with whole body imaging to consider the sporadic and random nature of initial onset locations of atrophy, while also observing the atrophy progression of critical areas such as the glossopharyngeal muscles, diaphragm and heart.

CHAPTER 3

GLIOBLASTOMA MODEL

Disease Introduction

Observing the progress of cancer research over the past few decades is remarkable when considering the short time span and the amount of knowledge learned. Understanding of tumor genetics, microenvironment, progression, and causal factors has spurred a new respect for the complexity of the disease. A major variant of cancer that is in the spotlight and a focus of research is the Glioblastoma which can range in severity from Grade I – IV. Glioblastoma is one the most lethal forms of brain cancers which can have a survival rate of 1-2 years for Grade III-IV. There are many variations and sub-types of glioblastoma tumors, treatments that may work for some may not work for others. Classifications for many of the sub-types of Glioblastoma is based on their genetic, histologic, and apparent structural or functional characteristics [31]. Understanding of the genetics and tumor microenvironment (TME) presented by Quail and Joyce point out many of the players in the TME that allow for growth and survival, particularly the compromised cells like astrocytes, macrophages, microglia, and lymphocytes that are essentially hijacked to promote tumor survival and evolution by regulating expression pathways and evading the natural immune response [32]. Tumor survival is dependent of the amount of nutrients it can receive to grow, and this is achieved, in part, via upregulated angiogenesis [32].

There are many MRI techniques possible for the characterization of brain tumors from MRS to static contrast enhanced T_1 weighted images. Currently perfusion imaging is used to make parametric maps to aid in resection of the tumor, and to reliably identify

tumor progression and treatment response [13]. As noted in Chapter 1, the disruption of the BBB due to tumor associated angiogenesis is often a challenge for robust DSC-MRI measures of CBV. The disrupted BBB and immature vasculature allow for contrast agent to extravasate, introducing additional simultaneous T_1 and T_2* changes that can be leveraged for estimating MRC parameters like TRATE. In the original model in which TRATE was developed for Semmineh et al. showed the capability of TRATE to differentiate between C6 and 9L tumors in rats [15].

A key use of MRI in brain tumor patient care is the detection and monitoring of glioblastomas' response to treatment. Whether it's determining the response to chemotherapy or post-resection, it is important to detect a tumor recurrence early for better patient outcomes. One chemotherapeutic used commonly is temozolomide (TMZ) which utilizes the methylation of DNA to destroy tumor cells [33]. Effective TMZ treatment has been known to lower CBV values in the U251 brain tumor animal model implanted in rats [34]. In addition, TMZ has been shown to arrest growth of tumor cells, reduced proliferation, and induced apoptosis [35]. Although these examples are in rat models, similar results have been shown in mice [36].

Methods

Animal Model

In this study 12 immunodeficient mice (Taconic Laboratories) had tumors induced via intracranial injection with human glioblastoma cell line ATCC-U87 tumor cells at 6-weeks-old and were allowed to proliferate for two-weeks before treatment with TMZ began. The treatment regime consisted of a dose protocol of 50mg/kg five days a week. The control cohort included vehicle treatment with Orablend. All mice were imaged at 8-

weeks-old to assess tumor progression and at 11-weeks-old to determine tumor response to therapy. All experiments and care for the mice were carried out in accordance with our institution's animal care and use polices.

Image Acquisition

The mice were imaged with a 7 Tesla (T) Bruker Scanner utilizing a 72mm transmit and read surface coil. Similar to the protocol applied in Semmineh et al. a pre-contrast T_1 images was acquired using a Variable Recovery Time (VTR) sequence with parameters: Repetition Times TR = [250ms, 500ms, 1000ms, 1500ms, 3000ms, 5000ms] TE = 11ms, FOV = 20 mm^2, Slice Thickness = 0.5mm, FA = 90°, Matrix = 200x200x4. Once the T_1 map was acquired, a DSC sequence was acquired using a multi-Echo GESFIDE sequence was acquired with the following parameters: TR = 350ms, 8 Echoes with spacing 4.86ms with start TE_1 = 3.8ms and end TE_8 = 46.6ms, FOV = 20mm^2, Slice Thickness = 0.5mm; FA = 90°, Dynamics = 45, Matrix = 100x100x4x45. A 0.2mM/kg dose of the contrast agent, Gadavist, was injected during the scan. To administer the contrast, a tail vein catheterization was performed to allow for an injection administered from a Genie Touch Syringe Pump (Lucca Technologies) at a rate of 1ml/min. The contrast was administered after an adequate baseline around 5-10 dynamics or 8-9min into the scan, and scanning was complete after 45 dynamics or 26 minutes.

Data Analysis

A similar analysis to that used in Chapter 2 was implemented, except ROIs were drawn to encompass signal enhancing regions of the brain. Care was taken to avoid necrotic regions, in some cases necrosis of the region was too advanced causing the data point to be removed.

Results

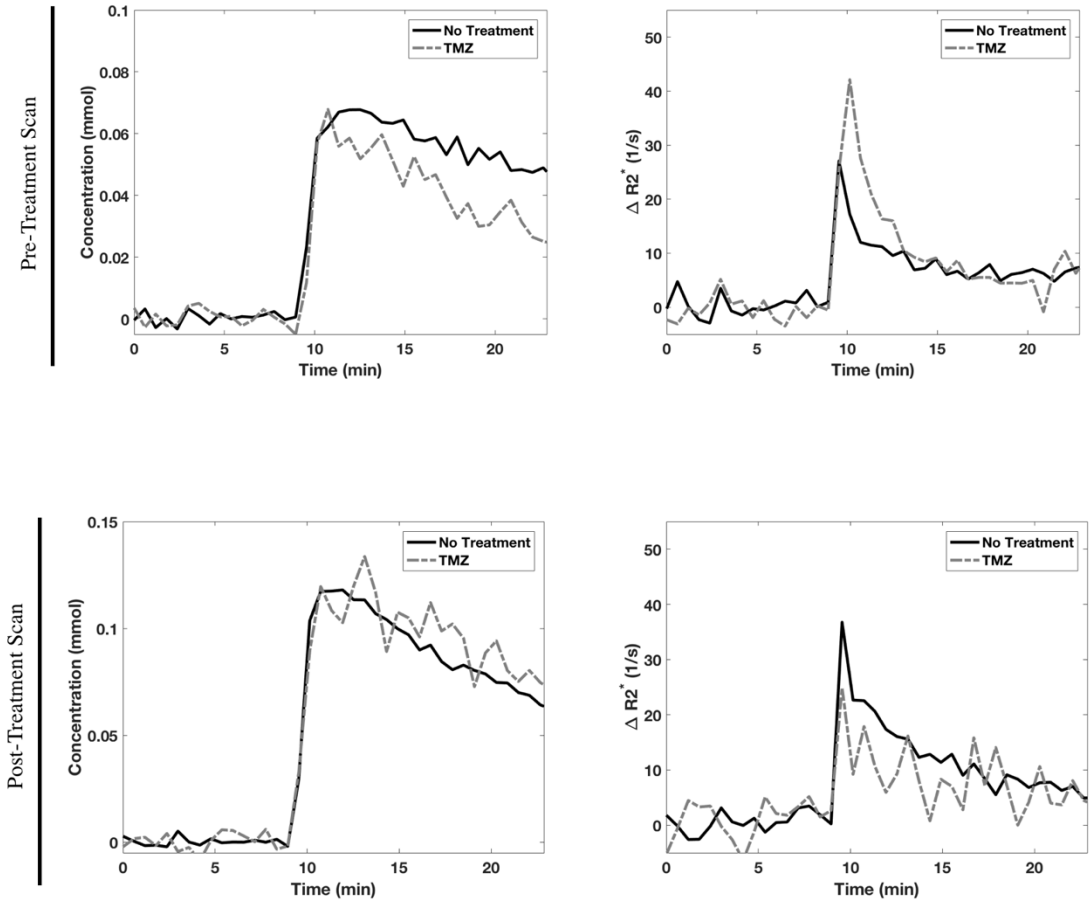

Figure 3.1 – Representative concentration and ΔR_2^* time profiles in enhancing tumor region.

Figure 3.1 shows examples of the dynamic concentration and ΔR_2^* curves obtained. Concentration profiles are reasonable and match prior studies but, interestingly, the magnitude of the T_2^* effects in brain tumors decay much more rapidly than observed in muscle (Figure 2.1). Similar to the challenges noted in the ALS study, the administered doses were variable and those represented in the figure were selected from each group based on the distance from the mean of the distribution.

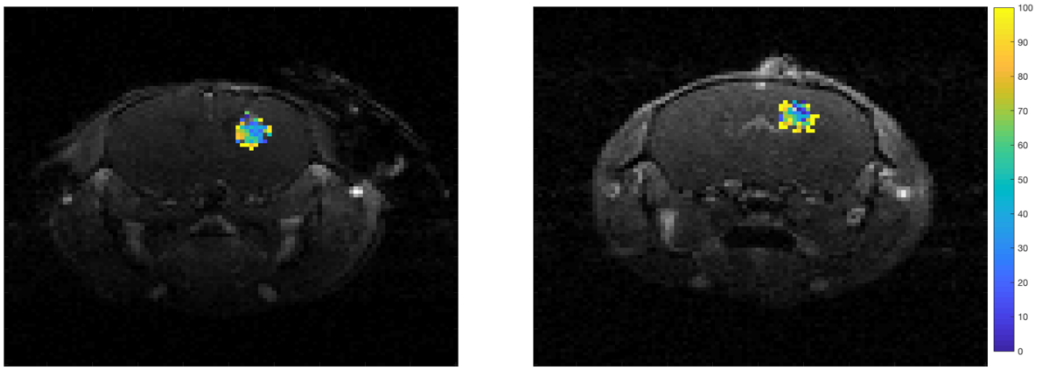

No Treatment TMZ Treatment

Figure 3.2 –TRATE maps in Non-TMZ treated and TMZ treated sample mice

From Figure 3.2 we can see the TRATE spatial distribution for one mouse in each group.

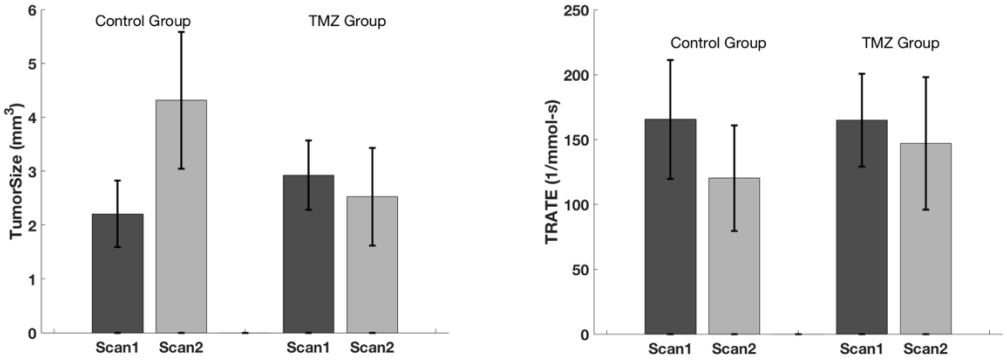

Figure 3.3 – Bar Graphs of Tumor Size and Averaged ROI TRATE Values

Figure 3.3 shows the bar graphs of tumor size and averaged TRATE values in the signal enhancing region where Scan 1 had six Control and five TMZ treated, and Scan2 had five Controls and TMZ treated mice. From the tumor size graph, we are seeing comparable results to that of Rao et. al. where the untreated mouse tumors are growing significantly and the TMZ treated mouse tumor growth was halted. Pre-treatment TRATE values between the two cohorts of animals were consistent. Surprisingly, TRATE values exhibited a non-significant decrease in both cohorts of animals after treatment with both

vehicle and TMZ. Despite this change in average scores for TRATE between the two, a two-sample t-test with 0.05 significance values yielded a failure to reject to the null hypothesis of the means being equal.

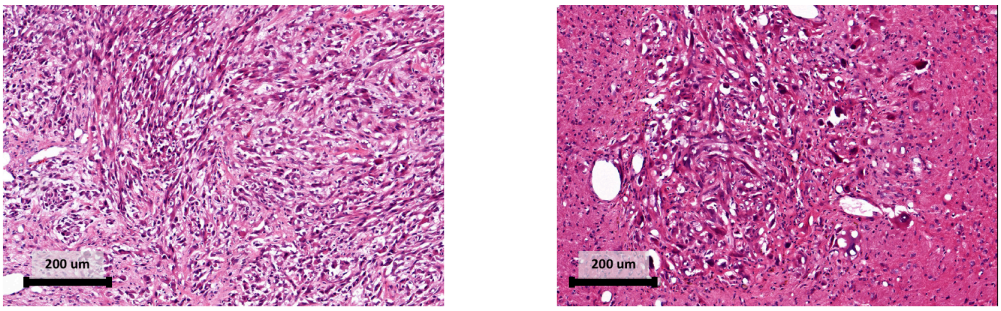

Control TMZ

Figure 3.4 – Hematoxylin and Eosin Stain of Tumor Samples

Figure 3.4 provides the histology for the treated and untreated tumors. In the control case we can see smaller tumor cells and a sparse distribution, while in the TMZ case we see larger tumor cells and a more clustered cell grouping. It is still not clear, whether there is a significant structural difference between the two.

Discussion

Considering the results, it is difficult to determine whether TRATE is detecting the cellular changes in response to Temozolomide. It is clear that a more detailed analysis of the histologic features and their differences before and after vehicle and TMZ treatment is necessary in order to fully interpret the TRATE results. Unfortunately, we do not have pre-treatment histology images for comparison in each cohort which makes it impossible to know if the underlying pathology changed between time points. It is feasible that the use of region of interest analysis in this study confounds the use of TRATE as a marker of treatment response because information about regional and individual heterogeneity is

lost. For example, animal models of brain cancer have increasing amounts of focus necrosis during tumor growth and that would tend to reduce TRATE values and could mimic treatment-induced cell death. Voxel-wise changes in biomarker data, a method called parametric response mapping, has shown increased predictive ability in brain cancer patients undergoing therapy, as compared to traditional ROI analysis. Future studies will seek to implement this method for the TRATE data collected herein.

Conclusion

TRATE has shown the capability of differentiating between brain tumor cell types in prior studies but did not show efficacy for detecting treatment induces changes. If TRATE ultimately provides sensitivity to treatment response in future studies, it can easily be acquired as part of a multi-echo perfusion scan that are acquired routinely. Ultimately, while preclinical studies of this nature are useful for characterizing the biophysical basis of contrast mechanisms like MRC, clinical studies are required to assess their true potential to alter therapeutic decisions. Interestingly, such clinical studies are surprisingly easier than the animal studies conducted herein due to easier contrast agent injections, higher contrast to noise and much larger tumor volumes.

CHAPTER 4

CONCLUSION

The development of minimally invasive biomarkers is an important field of research for prognosis and detection. Non-invasive means such as MRI allow for a higher frequency of sampling patient's disease progression. TRATE should be seen a biomarker that adds sub-voxel cellular structural information to already established quantitative assays of diseased tissues. In the case of muscle dystrophies, TRATE can be utilized as a prognosis tool to assess the degree of atrophy or wasting on the cellular level. In the field of the cancer, TRATE can be seen as an additional classification tool to established quantitative markers that interrogate tumors. While TRATE cannot replace histology, it is possible to glean a sense of underlying cellular structure and use this information to determine care prior to biopsy of tumor or serum analysis. TRATE has a series of milestones to achieve prior to being widely accepted, such as clinical validation, advanced histologic conformation, and applications in other disease states. To TRATE's benefit it does not require major changes in imaging protocols in the case of gliomas to be adopted since quantitative perfusion imaging is already implemented in many treatment routines. Moving forward, it will be important to create more efficacy and validation experiments to further understand the nuances of this technique. Currently, TRATE is being applied to human ALS studies and is showing promising and parallel results to the study conducted in this work. Overall, TRATE is in a nascent stage of development but shows tremendous promise and potential impact.

REFERENCES

[1] Edelman R. The History of MR Imaging as through the Pages of Radiology.2014.

[2] Haacke M, Brown R, Thompson M, Venkatesan R. Magnetic Resonance Imaging: Physical Principles and Sequence Design. 1999.

[3] Helms G, Garea-Rodriguez E. Structural and Quantitative Neuroimaging of the Common Marmoset Monkey using a Clinical MRI system. J Neurosci Methods. 2013.

[4] Deistung A, Stefanescu MR. Structural and Functional Magnetic Resonance Imaging of the Cerebellum: Considerations for assessing Cerebellar Ataxias. Cerebellum 2016.

[5] Horská A, Barker PB. Imaging of Brain Tumors: MR Spectroscopy and Metabolic Imaging. Neuroimaging clinics of North America 20(3):293-310, 2010

[6] A. Villringer, B. R. Rosen, J. W. Belliveau, J. L. Ackerman, R. B. Lauffer, R. B. Buxton, Y:S. Chao, V. J. Wedeen, T. J. Brady. Dynamic imaging with lanthanide chelates in normal brain: contrast due to magnetic susceptibility effects. Magn. Reson. Med. 6,164-174, 1988.

[7] Yankeelov TE, Gore JC. Dynamic Contrast Enhanced Magnetic Resonance Imaging in Oncology: Theory, Data Acquisition, Analysis, and Examples. Current medical imaging reviews, 3(2):91-107, 2009.

[8] Østergaard, L. , Weisskoff, R. M., Chesler, D. A., Gyldensted, C. and Rosen, B. R. High resolution measurement of cerebral blood flow using intravascular tracer bolus passages. Part I: Mathematical approach and statistical analysis. Magn. Reson. Med., 36: 715-725, 1996.

[9] Tofts, P. S., Brix, G. , Buckley, D. L., Evelhoch, J. L., Henderson, E. , Knopp, M. V., Larsson, H. B., Lee, T. , Mayr, N. A., Parker, G. J., Port, R. E., Taylor, J. and Weisskoff, R. M. Estimating kinetic parameters from dynamic contrast-enhanced t1-weighted MRI of a diffusable tracer: Standardized quantities and symbols. J. Magn. Reson. Imaging, 10: 223-232, 1999.

[10] Landis, C. S., Li, X. , Telang, F. W., Coderre, J. A., Micca, P. L., Rooney, W. D., Latour, L. L., Vétek, G. , Pályka, I. and Springer, C. S. Determination of the MRI contrast agent concentration time course in vivo following bolus injection: Effect of equilibrium transcytolemmal water exchange. Magn. Reson. Med., 44: 563-574, 2000.

[11] Troprès, I. , Grimault, S. , Vaeth, A. , Grillon, E. , Julien, C. , Payen, J. , Lamalle, L. and Décorps, M. Vessel size imaging. Magn. Reson. Med., 45: 397-408, 2001.

[12] Yablonskiy, D. A. and Haacke, E. M. Theory of NMR signal behavior in magnetically inhomogeneous tissues: The static dephasing regime. Magn. Reson. Med., 32: 749-763, 1994.

[13] Stokes AM, Skinner JT, Yankeelov T, Quarles CC. Assessment of a Simplified Spin and Gradient Echo (sSAGE) Approach for Human Brain Tumor Perfusion Imaging. Magnetic resonance imaging ;34(9):1248-1255, 2016.

[14] Bell LC, Hu LS, Stokes AM, McGee SC, Baxter LC, Quarles CC. Characterizing the Influence of Preload Dosing on Percent Signal Recovery (PSR) and Cerebral Blood Volume (CBV) Measurements in a Patient Population With High-Grade Glioma Using Dynamic Susceptibility Contrast MRI. Tomography. 2017;3(2):89-95.

[15] Quarles CC, Gochberg DF, Gore JC, Yankeelov TE. A theoretical framework to model DSC-MRI data acquired in the presence of contrast agent extravasation. Phys Med Biol. ;54(19):5749-66. 2009.

[16] Semmineh NB, Xu J, Boxerman JL, Delaney GW, Cleary PW, Gore JC, et al. An Efficient Computational Approach to Characterize DSC-MRI Signals Arising from Three-Dimensional Heterogeneous Tissue Structures. PLoS ONE 9(1): e84764. 2014.

[17] Semmineh NB, Xu J, Skinner JT, et al. Assessing tumor cytoarchitecture using multi-echo DSC-MRI derived measures of the Transverse Relaxivity at Tracer Equilibrium (TRATE). Magnetic resonance in medicine;74(3):772-784, 2015.

[18] Zarei, S., Carr, K., Reiley, L., Diaz, K., Guerra, O., Altamirano, P. F., … Chinea, A. A comprehensive review of amyotrophic lateral sclerosis. Surgical Neurology International, 6, 171, 2015.

[19] Leigh, P., Abrahams, S., Al-Chalabi, A., Ampong, M., Goldstein, L., Johnson, J., … Willey, E. THE MANAGEMENT OF MOTOR NEURONE DISEASE. Journal of Neurology, Neurosurgery, and Psychiatry, 74(Suppl 4), iv32–iv47, 2003.

[20] Mehta, P., Horton, K., Kasarskis, E., Tessaro, E., Eisenberg, M.S., Laird, S., Iskander, J., (2017). CDC Grand Rounds: National Amyotrophic Lateral Sclerosis (ALS) Registry Impact, Challenges, and Future Directions. MMWR Morb Mortal Wkly Rep; 66(50): 1379–1382, 2017.

[21] Matthew C Kiernan, Steve Vucic, Benjamin C Cheah, Martin R Turner, Andrew Eisen, Orla Hardiman, James R Burrell, Margaret C Zoing. Amyotrophic lateral sclerosis, The Lancet, Volume 377,Issue 9769,Pages 942-955,ISSN 0140-6736, 2011.

[22] Gupta A, Nguyen TB, Chakraborty S, Bourque PR., Accuracy of Conventional MRI in ALS. Can J Neurol Sci;41(1):53-7, 2014.

[23] Chen, J., Kostenko, V., Pioro, E., Trapp, B. MR Imaging–based Estimation of Upper Motor Neuron Density in Patients with Amyotrophic Lateral Sclerosis: A Feasibility Study. Radiology, 2018.

[24] Müller, H.-P., Agosta, F., Riva, N., Spinelli, E. G., Comi, G., Ludolph, A. C., … Kassubek, J. Fast progressive lower motor neuron disease is an ALS variant: A two-centre tract of interest-based MRI data analysis. NeuroImage: Clinical, 17, 145–152, 2018.

[25] Ferraro, P. M., Agosta, F., Riva, N., Copetti, M., Spinelli, E. G., Falzone, Y., … Filippi, M. Multimodal structural MRI in the diagnosis of motor neuron diseases. NeuroImage : Clinical, 16, 240–247, 2017.

[26] Evans, M. C., Serres, S., Khrapitchev, A. A., Stolp, H. B., Anthony, D. C., Talbot, K., … Sibson, N. R. T2-Weighted MRI Detects Presymptomatic Pathology in the SOD1 Mouse Model of ALS. Journal of Cerebral Blood Flow & Metabolism, 34(5), 785–793, 2014.

[27] Heiko G. Niessen, Frank Angenstein, Kerstin Sander, Wolfram S. Kunz, Marko Teuchert, Albert C. Ludolph, Hans-Jochen Heinze, Henning Scheich, Stefan Vielhaber, In vivo quantification of spinal and bulbar motor neuron degeneration in the G93A-SOD1 transgenic mouse model of ALS by T2 relaxation time and apparent diffusion coefficient, Experimental Neurology,Volume 201, Issue 2,Pages 293-300,ISSN 0014-4886, 2006.

[28] Marco A. Marra, Linda Heskamp, Karlien Mul, Saskia Lassche, Baziel G.M. van Engelen, Arend Heerschap, Nico Verdonschot, Specific muscle strength is reduced in facioscapulohumeral dystrophy: An MRI based musculoskeletal analysis, Neuromuscular Disorders, ISSN 0960-8966, 2017.

[29] A. Eresen, S. McConnell, S. M. Birch, J. F. Griffin, J. N. Kornegay and J. X. Ji, "Tissue classification in a canine model of Duchenne Muscular Dystrophy using quantitative MRI parameters," 2017 39th Annual International Conference of the IEEE Engineering in Medicine and Biology Society (EMBC), Seogwipo, pp. 4066-4069, 2017.

[30] Kiselev, V.G. On the theoretical basis of perfusion measurements by dynamic susceptibility contrast MRI. Magn. Reson. Med., 46: 1113–1122, 2001.

[31] Bonaldo P, Sandri M. Cellular and molecular mechanisms of muscle atrophy. Disease Models & Mechanisms;6(1):25-39. 2013.

[32] Straub, V. , Donahue, K. M., Allamand, V. , Davisson, R. L., Kim, Y. R. and Campbell, K. P. Contrast agent-enhanced magnetic resonance imaging of skeletal muscle damage in animal models of muscular dystrophy. Magn. Reson. Med., 44: 655-659, 2000.

[33] Quail DF, Joyce JA. The microenvironmental landscape of brain tumors. Cancer cell; 31(3):326-341, 2017.

[34]Gilbertson R, Rich J. Making a tumor's bed: glioblastoma stem cells and the vascular niche. Nature Reviews Cancer;Volume 7, pages 733–736, 2000.

[35] Friedman HS, Kerby T. and Calvert H. Temozolomide and Treatment of Malignant Glioma. ClinCancerRes; (6) (7) 2585-2597, 2000.

[36] Corroyer-Dulmont A, Pérès EA, Petit E, et al. Detection of glioblastoma response to temozolomide combined with bevacizumab based on µMRI and µPET imaging reveals [18F]-fluoro-l-thymidine as an early and robust predictive marker for treatment efficacy. Neuro-Oncology;15(1):41-56, 2013.

[37] Rao JU, Coman D, Walsh JJ, Ali MM, Huang Y, Hyder F. Temozolomide arrests glioma growth and normalizes intratumoral extracellular pH. SciRep; 7:7865,2017.

[38] Towner RA, Ihnat M, Saunders D, et al. A new anti-glioma therapy, AG119: pre-clinical assessment in a mouse GL261 glioma model. BMC Cancer;15:522, 2017.

APPENDIX A
PROCESSING CODE

```
function [] = fidreader;
%%%%%%%%%%%%%%%Generates Signals and Parameters files for all relevent
scans
%%%%%%%%%%%%%AF Q1 2018 Adaptation from BrukerImageProcessor AM Stokes
%%%%%%%%%%%Make sure fid is 16 bit otherwise manually read the file as
%%%%%%%%%%%32bit with fread function
%Get the current directory (Mouse/Patient File)
dirname = pwd;
%%% Search through directory for scans
    for a = 1:40
        try
            BRUKER_FILE1=[dirname '/' num2str(a)
'/pdata/1/2dseq'];   %This program uses the processed 2dseq file.
            pars = readnmrpar([BRUKER_FILE1(1:end-13) 'method']);
            display(['The method for scan number ' num2str(a) ' is '
pars.Method '.']);
        catch
        end
    end
%%%%%Choose the scans you want processed
scans = input('Enter the Scan number you would like processed in a
vector ex : [ 1 ...n]');
%%%Processing For loop
for k = 1: length(scans)
    clear BRUKER_FILE1 pars Nechoes
    BRUKER_FILE1=[dirname '/' num2str(scans(k)) '/pdata/1/2dseq'];
    pars = readnmrpar([BRUKER_FILE1(1:end-13) 'method']);
    visu = readnmrpar([BRUKER_FILE1(1:end-5) 'visu_pars']);
    NpointRD=pars.PVM_Matrix(2);       %Size of read direction matrix
    NpointPE=pars.PVM_Matrix(3);      %Number of phase encode steps
    ns = pars.PVM_SPackArrNSlices(2); %Slices
    if length(pars.PVM_Matrix) > 3 %%for 3D acq
        ns=pars.PVM_Matrix(4);
    end
%%% Account for the Possible Inputs
switch pars.Method
    case 'gESFIDE'
        Nechoes = pars.NEchoes;
        dyn = pars.PVM_NRepetitions;
    case 'MGE'
        Nechoes = pars.PVM_NEchoImages;
        dyn = pars.PVM_NRepetitions;
    case 'MSME'
        Nechoes = pars.NEchoes;
        dyn = pars.PVM_NRepetitions;
    case 'RAREVTR'
        Nechoes = pars.MultiRepetitionTime(1);
        dyn = pars.PVM_NRepetitions;
        pars.RECO_wordtype(2:3) = '16';
    case 'RARE'
        dyn = pars.PVM_NRepetitions;
    case 'EPI'
        dyn = 0;
        Nechoes = pars.PVM_NRepetitions;
    case 'DtiStandard'
        dyn = 0;
        ns = pars.PVM_SPackArrNSlices(2); %Slices
```

```
        Nechoes = pars.PVM_DwNDiffExp;
        NpointRD=visu.VisuCoreSize(2);       %Size of read direction
matrix
        NpointPE=visu.VisuCoreSize(3);
    case 'DtiEpi'
        dyn = 0;
        ns = pars.PVM_SPackArrNSlices(2); %Slices
        Nechoes = length(pars.PVM_DwEffBval)-1;
        NpointRD = pars.PVM_Matrix(3);
        NpointPE = pars.PVM_Matrix(2);



end
%%%%Assigning bit integer
try
    pars.RECO_wordtype;
catch
    pars.RECO_wordtype(2:3) = '16';
end
%%%%%%Read Fid
fid1=fopen(BRUKER_FILE1,'r','l');   %Open fid
fidmix1=fread(fid1,inf,['int' pars.RECO_wordtype(2:3)]);    %Read fid
data as single line
if dyn>2

signal=reshape(fidmix1,NpointRD,NpointPE,Nechoes,ns,dyn);    %Reshape
data into read and phase encode directions
        else
        signal=reshape(fidmix1,NpointRD,NpointPE,ns,Nechoes);%Reshape
data into read and phase encode directions
end
signal = imrotate(signal,270);  %Rotate image 270 degrees
signal = fliplr(signal);        %Flip image left to right
cd([dirname '/' num2str(scans(k))])
twodseqcorr(signal,pars)
cd([dirname])
  save([dirname '/' num2str(scans(k)) '/signal.mat'],'signal','pars')
end
    clear k
end
function [T2data] = T2mapp(signal,pars)
%% 2dseq Correct
function [] = twodseqcorr(signal,pars)
Size = size(signal);
Visu = readnmrpar('pdata/1/visu_pars');
VisuSlopeConsant = Visu.VisuCoreDataSlope(2:end);
VisuOffeset = Visu.VisuCoreDataOffs(2:end);
if length(Size)>4
    [nx, ny, ne, nz, dyn] = size(signal);
    VisuSlopeConsant = reshape(VisuSlopeConsant,[ne nz dyn]);
    VisuOffeset = reshape(VisuOffeset,[ne nz dyn]);
    VisuSlopeMatrix = ones(nx,ny,ne,nz,dyn);
    VisuOffesetMatrix = ones(nx,ny,ne,nz,dyn);
    for j  = 1:dyn
        for k = 1:nz
```

```
            for l = 1:ne
               VisuSlopeMatrix(:,:,l,k,j) =
squeeze(VisuSlopeMatrix(:,:,l,k,j)) *VisuSlopeConsant(l,k,j);
            end
        end
    end
     for j  = 1:dyn
        for k = 1:nz
            for l = 1:ne
               VisuOffesetMatrix(:,:,l,k,j) =
squeeze(VisuOffesetMatrix(:,:,l,k,j)) *VisuOffeset(l,k,j);
            end
        end
    end
else
    [nx, ny, nz, ne] = size(signal);
    VisuSlopeConsant = reshape(VisuSlopeConsant,[nz ne]);
    VisuOffeset = reshape(VisuOffeset,[nz ne]);
    VisuSlopeMatrix = ones(nx,ny,nz,ne);
    VisuOffesetMatrix = ones(nx,ny,nz,ne);
    for l = 1:ne
        for k = 1:nz
        VisuSlopeMatrix(:,:,k,l) = squeeze(VisuSlopeMatrix(:,:,k,l))
*VisuSlopeConsant(k,l);
        end
    end
    for l = 1:ne
        for k = 1:nz
        VisuOffesetMatrix(:,:,k,l) =
squeeze(VisuOffesetMatrix(:,:,k,l)) *VisuOffeset(k,l);
        end
    end
end
Final2dseq = signal.*VisuSlopeMatrix+VisuOffesetMatrix;
signal = Final2dseq;
save('signalcorr.mat','pars','signal')
function []  = T1mapp(signal,pars)

%% T1 Processing
%%%%%%%%%%%%%%%%%%%AF Q1 2018 Adaptation of BrukerImageProccessor A.M
Stokes %%%%%%%%%%%%%%%%
%Takes in VTR volume and fits a T1 curve using lsqcurvefit
%You need an ROI, Signal Volume, and parameter file
%Get ROI using ROIgen %Get Signal Volume and Pars from FID2Sig
%% Pre allocating
TR = pars.MultiRepetitionTime(2:end);
NTR = pars.NumT1Exps;
[nx, ny, ns, ne] = size(signal);
T1_map = zeros(nx,ny,ns);
S0_map = zeros(nx,ny,ns);
error_map = zeros(nx,ny,ns);
LB = [];
UB = [];
options = optimset('TolFun',1e-9,'Tolx',1e-
9,'MaxIter',1000,'Display','off','Algorithm','levenberg-marquardt');
%% For Loop
        parfor z = 1:ns
```

```
            disp(z)
            for x = 1:nx
                for y = 1:ny
                        data= squeeze(signal(x,y,ns,:));
                        voxel_data = data;
                        params = [2000 max(voxel_data)]; %initial
guesses [T1 So]
                        [output, resid] =
lsqcurvefit('t1_vtr_cf',params,TR',voxel_data,LB,UB,options);
                        T1_map(x,y,z) = output(1);
                        S0_map(x,y,z) = output(2);
                        error_map(x,y,z) = resid;
                end
            end
        end
        figure;imagesc(T1_map(:,:,3),[0 4000]);title(['T_1 map for
slice ' num2str(2)]);colorbar; axis square off;
        disp('Finished processing T1 maps, saving now')
        dirname = pwd;
        save([dirname '/T1map.mat'],'T1_map','S0_map','error_map');
    end




%% T2 Processing
%%%%%%%%%%%%%%AF Q1 2018 Adaptation of Bruker Image Processor A.M
Stokes
%Takes in GESFIDE Volume and fits for T2 and T2* using lsqcurve and
%Piecewise Equation Ma. Wheril
%% Pre Allocating
[nx, ny, ne, ns, NTR] = size(signal);
S1m = nan(nx,ny,ns,NTR);
S2m = nan(nx,ny,ns,NTR);
R2sm = nan(nx,ny,ns,NTR);
R2m = nan(nx,ny,ns,NTR);
NGE = pars.GESFIDE_NGE;
NpSE = pars.GESFIDE_NpSE;
SE_TE_ms = pars.GESFIDE_EchoTimeSE;
xdata = pars.EffectiveTE(2:end);
LB = [0 0 0 0];
UB = [Inf Inf Inf Inf];
options = optimset('TolFun',1e-9,'Tolx',1e-
9,'MaxIter',2000,'Display','off');
%% Fitting
%4p for baseline
% R2 and R2* output in 1/s
    parfor zz = 1:NTR
        disp(zz)
        for z = 1:ns

            for y = 1:ny
                for x = 1:nx
                    if isnan(signal(x,y,1,z,zz))

                    else
```

```
                        map = squeeze(signal(x,y,:,z,zz));
                        x0 = [max(map) max(map) 20 40]; %initial guesses
[S1, S2, R2*, R2]
                        ydata = squeeze(signal(x,y,:,z,zz));
                        [par4, resnorm] =
lsqcurvefit('gesfide4p',x0,xdata,ydata',LB,UB,options,SE_TE_ms,NGE,NpSE
);
                        S1m(x,y,z,zz) = par4(1);
                        S2m(x,y,z,zz) = par4(2);
                        R2sm(x,y,z,zz)= par4(3);
                        R2m(x,y,z,zz) = par4(4);
                        %resnormew(x,y,z,zz) = resnorm;
                    end
                end
            end
        end
    end
dirname = pwd;
%Creating Structure to save T2 T2* R2 R2* S1 S2
T2data.S1 = S1m;
T2data.S2 = S2m;
T2data.R2 = R2m;
T2data.R2s = R2sm;
%T2data.resnom = resnormew;
%Saving Strucuture
%save([dirname  '/T2datacorrbothlegs.mat'], 'T2data')
%fprintf('Mapping Complete and Files Saved')
end

function [Conc] = Conc(T1,S1,T2pars)
%%%%%%%%%%%%%%%%%%%%%%Concetration and DR1 Calculator%%%%%%%%%%%%%%%%
%%%%%%%%%%%%%%%%%%%%%%AF Q2 2018%%%%%%%%%%%%%%%%%%%%%%%%%%
%%%%%%%Takes in T1map and S1 from GESFIDE Output to Calculate DR1 and
%%%%%%%Concentration. This Currently is applied for Gadvist Relaxivity
%%%%%%%change accordingly
[S1nx, S1ny, S1nz, S1r] = size(S1);
r1 = 3.2;%relaxivity mmol/s
TR = (T2pars.PVM_RepetitionTime); %ms
alpha = str2double(T2pars.ExcPulse(11:12));%degrees
NT1 = zeros(S1nx,S1ny,S1nz);
NT1 = T1;
%Refocusepulse = str2num(pars.RefPulse(27:29));
%TE = T2pars.PVM_EchoTime;%ms
%Resizing T1map to Fit T2map

%NT1(:,:,k) = imresize3(T1, [S1nx S1ny S1nz],'Method','linear');%ms

S_ = squeeze(mean(S1(:,:,:,1:4),4));%Acquiring Signal Baseline Average
of 10 Dynamics
psi = S_.*(1-(exp(-TR./NT1).*cosd(alpha)));%Numerator of S0 equation
usp = (1-exp(-TR./NT1).*sind(alpha));%Denominator of S0equation
S0 = (psi./usp);
parfor j = 1:S1r
    disp(j)
            %R1calc
```

```
            R1(:,:,:,j) = -(1/TR).*log((((S0.*sind(alpha) -
S1(:,:,:,j))).*(S0.*sind(alpha)-S1(:,:,:,j).*cosd(alpha))));


end
R10 = squeeze(mean(R1(:,:,:,1:4),4));%R1 pre
clear j
parfor j = 1:S1r
DR1(:,:,:,j) = squeeze(R1(:,:,:,j))-R10;%
end
Conc = DR1.*1000/r1;
%save('conc.mat','R1','DR1','Conc','r1')

end
%%

%%%%%%%%%%%%%% TRATE Map%%%%%%%%%%%%%%%%%%%%%%%%%
%%%%%%%%%%%%%%%% AF Q1 2017%%%%%%%%%%%%%%%%%%%%%%%%%%%%
clear
clc
load('4/T1map.mat');
load('5/T2data.mat');
for k = 1:4
NT1(:,:,k) = imresize(T1_map(:,:,k), [98 98]);
end
R2s = 1./T2data.T2s;%ms
BRUKER_FILE1=['5/pdata/1/2dseq'];
pars = readnmrpar([BRUKER_FILE1(1:end-13) 'method']);
%% Calculate S0 of GE for R1 Solving
%Landis Eq (4) Solving for S0
S1 = T2data.S1;
[nx, ny, nz, r]  =size(S1);
%Constants
TR = (pars.PVM_RepetitionTime); %ms
alpha = 90; %degrees
TE = (pars.PVM_EchoTime); %ms
disp('R1calc')
%S0 Clac
%Baseline Signal
 S_ = squeeze(mean(S1(:,:,:,1:10),4));
 %Getting T1
 T1 = NT1(:,:,:);%ms
 %Calculating Numerator
 psi = S_.*(1-(exp(-TR./T1).*cosd(alpha)));
 %Calculating Denominator
 usp = (1-exp(-TR./T1))*sind(alpha);
 %S0
 S0 = (psi./usp);
 %R1 Calculation
parfor j = 1:r
    disp(j)
            %R1calc
            %Numerator
            psi2 = (S0.*sind(alpha)-squeeze(S1(:,:,:,j)).*cosd(alpha));
            %Denominator
            usp2 = (S0.*sind(alpha)-squeeze(S1(:,:,:,j)));
```

```
            %R1
            R1(:,:,:,j) =
(1/TR).*log((psi2./usp2).*exp(TE.*squeeze(R2s(:,:,:,j))));%1/ms
%%% Compare with T2s and w/o
end
clear j g h k
%R10
    R10 = squeeze(mean(R1(:,:,:,1:10),4));
disp('DR1 Calc')
parfor j = 1:r
disp(j)
%Calcualte Delta R1
DR1(:,:,:,j) = squeeze(R1(:,:,:,j))-R10;
end
%%
r1 = 3.2; %Same paper as before but the concentration 4mol at 7T Units
~ 1/mmol-s
%Eq 12.1  Yankeelov Pickens Price Quantitative MRI in Cancer Using
Signal from S1 (90 flip Echo) of Gesfide Output
Conc= (DR1.*1000)./r1; % (1/ms)/(1/mMol-s) -->*1000 ---> (1/s)/(1/mmol-
s) --> mmol
disp('DR2scalc')
%R20 Calculation 10 base line points
R2s0 = squeeze(nanmean(R2s(:,:,:,1:8),4));
DR2s = R2s-R2s0;
%TRATE
TrateDR2s = squeeze(mean(DR2s(:,:,:,end-5:end),4)).*1000;
TrateConcmap = abs(squeeze(mean(Conc(:,:,:,end-5:end),4)));
TrateConc = squeeze(mean(Conc(:,:,:,end-5:end),4));
Trate= abs(TrateDR2s./TrateConc);
%save('Tratemap.mat','Trate')
%% Plotting Sanity Check
figure
imagesc(abs(Trate(:,:,2)),[0 300])
figure
histogram(abs(Trate),'BinLimits',[5 250])


function [] = TRATE(Conc,R2s)
%%%%%%%%%%%%%%%%%%%%%%%%TRATE Calculator%%%%%%%%%%%%%%%%%%%%%%%%%%%
%%%%%%%%%%%%%%%%%%%%%% AF Q2 2018%%%%%%%%%%%%%%%%%%%%%%%%%%%%%%%%%
%%%%%%%%%%Takes in Concentration time curve and DR2s Time Curve to
%%%%%%%%%%calculate a map of TRATE values
[nx, ny, nz, dyn] = size(R2s);
R2ss = nan(nx,ny,nz,dyn);
%Temporal Smoothing MWA size 3
for k = 1:nz
    for h = 1:ny
        for g = 1:nx
            R2ss(g,h,k,:) = smooth(R2s(g,h,k,:));
        end
    end
end
%Concentration Filter Removing Outliers
Conc = real(Conc);
Cmax = squeeze(max(Conc,[],4));
Cmaxm = nanmean(reshape(Cmax,[98*98*6 1]));
```

```
Cmaxstd = nanstd(reshape(Cmax,[98*98*6 1]));
Cmax(Cmax>(Cmaxm+Cmaxstd)) = nan;
Cmax(Cmax<(Cmaxm-Cmaxstd)) = nan;
Cmaxm2 = nanmean(reshape(Cmax,[98*98*6 1]));
Cmaxstd2 = nanstd(reshape(Cmax,[98*98*6 1]));
B = nan(98,98,6);
B(Cmax>0) = 1;
R2ss0 = squeeze(nanmean(R2ss(:,:,:,1:7),4));
for k = 1:dyn
    DR2ss(:,:,:,k) = R2ss(:,:,:,k)-R2ss0;
end
A = nanmean(DR2ss(:,:,:,end-7:end),4)- nanmean(DR2ss(:,:,:,1:7),4);
%Removing Negative Curves
A(A<0) = nan;
A(A>0) = 1;
%Combining Filters
A = A.*B;
for k = 1:dyn
    DR2ss(:,:,:,k) = DR2ss(:,:,:,k).*A;
end
for k = 1:dyn
    Conc(:,:,:,k) = Conc(:,:,:,k).*A;
end
%TRATE Calculation
TrateDR2ss = squeeze(nanmean(DR2ss(:,:,:,end-3:end),4));
TrateConc = squeeze(nanmean(Conc(:,:,:,end-3:end),4));
Trate= TrateDR2ss./TrateConc;
save('TRATEresultpatch.mat','Trate','TrateConc','TrateDR2ss')
end
```